Available online at www.sciencedirect.com

jmr&t Journal of Materials Research and Technology

journal homepage: www.elsevier.com/locate/jmrt

Effects of layer thickness on deformation-induced martensite transformation and tensile behaviors in a multilayer laminate

Yanke Liu [a,b,1], Guohao Qin [a,b,1], Wei Wang [a,*], Yan Ma [c], Muxin Yang [a], Sihai Jiao [d], Xiaolei Wu [a,b], Fuping Yuan [a,b,**]

[a] State Key Laboratory of Nonlinear Mechanics, Institute of Mechanics, Chinese Academy of Sciences, No.15, North 4th Ring, West Road, Beijing 100190, China

[b] School of Engineering Sciences, University of Chinese Academy of Sciences, Beijing 100190, China

[c] Department of Materials Science and Engineering, Mechanical Behavior Division of Shenyang National Laboratory of Materials Science, City University of Hong Kong, Hong Kong, China

[d] Baosteel Research Institute, Baoshan Iron & Steel Co., Ltd., Shanghai 201900, China

ARTICLE INFO

Article history:
Received 4 April 2023
Accepted 2 July 2023
Available online 6 July 2023

Keywords:
Multilayer laminates
Layer thickness
Strain gradients
Strain hardening
Deformation-induced martensite transformation
Dislocation behavior

ABSTRACT

Multilayer laminates with a 304 stainless steel as surface layers and with a low C steel and a medium-Mn steel as alternating central layers have been developed in the present study. The number of interfaces and the layer thickness have been varied, while maintaining the similar microstructures for each layer. The uniform elongation is observed to increase from 10.1% to 37.8%, and the product of strength and elongation is found to increase from 13.6 GPa·% to 36.8 GPa·% monotonically with decreasing layer thickness in multilayer laminates, while the yield stress remains almost constant. Firstly, deformation-induced martensite transformation is significantly promoted with decreasing layer thickness. Secondly, the more interfaces can induce the accumulation of higher density of geometrically necessary dislocations, resulting in better mechanical properties. Lastly, the main cracks nucleate and propagate at the interfaces of low C steel layers and medium Mn steel layers, thus the samples with smaller layer thickness have more interfaces and require more energy consumption during the micro-fracture process, resulting in better tensile performance.

1. Introduction

Strength and ductility, the most important two parameters for structural applications, are mutually exclusive in general for metals with homogeneous structures [1,2]. The attempt in enhancing yield strength by cold working or grain refinement, is inevitably leading to a loss of tensile ductility [3,4]. Imparting large ductility to high strength metals by novel designs is a challenge and is always desirable for practical

* Corresponding author.
** Corresponding author.
E-mail addresses: wangwei2@imech.ac.cn (W. Wang), fpyuan@lnm.imech.ac.cn (F. Yuan).
[1] These two authors contributed equally to this work.
https://doi.org/10.1016/j.jmrt.2023.07.006

applications. Heterogeneous structures, a new class of materials with different domains in which mechanical properties (such as strength/hardness) are dramatically varied, have been considered as a promising strategy to obtain both high strength and large ductility [5–21]. Stress/strain partitioning among various domains, strain gradients across the domain boundaries, pile-up of geometrically necessary dislocations (GNDs) near the domain boundaries and hetero-deformation-induced (HDI) hardening have been found to be the origins for the extraordinary mechanical properties in metals with heterogeneous structures [7,10,13,22,23].

In last two decades, several heterogeneous structures, such as gradient structures [5–8], heterogeneous grain structures [9–11], nanodomained structures [12], and heterogeneous lamella structures [13–21], have been proposed to achieve excellent synergy of strength and ductility in metals and alloys. As one type of heterogeneous lamella structures, multilayer laminates recently have attracted massive research interests due to their superior tensile properties by optimizing the parameters of microstructures, such as the layer thickness and the difference in strength/hardness across the layer interfaces [16,19–21,24–26]. Due to the strain gradients and the accumulations of GNDs at the layer interfaces, interface-affected-zone (IAZ) has been defined based on a dislocation ledge model, and the width of IAZ has been found to be several micrometers and to remain constant during tensile deformation [15,16,19]. Thus, the tensile ductility in multilayer laminates can be optimized 16 by adjusting layer thickness, since the IAZ area increases first with decreasing layer thickness, and then decreases with further reducing layer thickness due to the overlap of adjacent IAZs [19].

Moreover, the yield strength, the strain hardening ability and the uniform elongation have been found to be far beyond the predicted values by rule of mixture due to the HDI effects and the enhanced interface constraint effects [21]. Crystal plasticity finite element simulations based on 3D discrete dislocations have been conducted to reveal the extra strengthening/hardening mechanisms in the multilayer laminates [14], the results have indicated that the multilayer laminates can homogenize the plastic deformation in the brittle layers, weakening the effect of strain concentrations and delaying the strain instabilities in the brittle layers.

Among various steels, the medium-Mn transformation-induced-plasticity (TRIP) steels have been considered as the promising materials for structural applications demanding high strength, large ductility and high energy absorption, due to their strong strain hardening capacity by TRIP effect and their relative low cost [27–30]. Moreover, stainless austenitic steels [31–35] have also attracted extensive research interests due to their excellent mechanical properties by twinning-induced-plasticity (TWIP) and/or TRIP effects and their superior corrosion resistance. While, the possible effects of layer thickness on deformation-induced martensite transformation and tensile behaviors in the multilayer laminates with the medium-Mn TRIP steels and the stainless steels are still unclear. For applications as structural materials under corrosion environment, multilayer laminates with a 304 stainless steel as surface layers and with a low C steel and a medium-Mn steel as alternating central layers, have been developed and fabricated by hot-rolled (HR) bonding in the present study. The number of interfaces and the layer thickness have been varied, while maintaining the similar microstructures for each layer during the HR bonding process. Then, effects of layer thickness on the TRIP effects and the tensile properties for the produced multilayer laminates have been studied, and the corresponding deformation mechanisms have been systematically revealed by the detailed microstructural characterizations.

2. Materials and experimental methods

2.1. Material

The chemical compositions of the investigated low C steel, the medium Mn steel and the 304 stainless steel are 1.0Mn-0.2C-0.02Ti-0.04Nb, 6.7Mn-0.46Al-0.28C and 19Cr–10Ni-1.2Mn-0.05C (all in mass % and with the balance of Fe), respectively. HR bonding was used to fabricate the multilayer laminates with the 304 stainless steel as surface layers and with the low C steel and the medium-Mn steel as alternating central layers. For convenience, the 304 stainless steel layer, the low C steel layer and the medium-Mn steel layer are denoted as "S-layer", "L-layer" and "M-layer", respectively. The initial thickness of the low C steel and the medium-Mn steel prior to hot rolling is about 4.5 mm, while that of the 304 stainless steel is about 1.1 mm. 4-layered, 6-layered, 10-layered and 18-layered laminates were fabricated by HR bonding between 1150 °C and 900 °C, and the HR slabs all have a final thickness of about 5.5 mm. The layer thicknesses for L-layers in 4-layered, 6-layered, 10-layered and 18-layered HR multilayer laminates are about 2.01, 1.27, 0.56, and 0.26 mm, respectively, and are about 2.07, 1.01, 0.49, and 0.25 mm for M-layers, respectively. The layer thicknesses for S-layers are all the same (about 0.61 mm) in 4-layered, 6-layered, 10-layered and 18-layered HR multilayer laminates. In order to produce good bonding interfaces with high bonding strength, the HR slabs were annealed at 1000 °C followed by fast cooling with a cooling rate of 30 °C/s and pickling. The schematic diagrams for the HR multilayer laminates are shown in Fig. 1(a). The HR multilayer laminates were annealed at an intercritical temperature of 640 °C for 30 min followed by water quenching, and then were subjected to cold rolling with a total thickness reduction of 73%. Two middle annealing processes with an annealing temperature of 600 °C for 10 min followed by air cooling, were carried out during cold rolling at thickness reductions of 27% and 45%, respectively. The thickness reduction ratios for individual layers in multilayer laminates were nearly the same during HR bonding and cold rolling. Finally, the cold-rolled (CR) sheets were intercritically annealed at 645 °C for 30 min followed by air cooling, and these sheets were denoted as CRA sheets for convenience. The schematic diagrams for the CR multilayer laminates are shown in Fig. 1(b). The layer thicknesses for L-layers in 4-layered, 6-layered, 10-layered and 18-layered CR multilayer laminates are about 610, 335, 140, and 75 μm, respectively, and are about 590, 280, 130, and 72 μm for M-layers, respectively. The layer thicknesses for S-layers are all the same (about 150 μm) in 4-layered, 6-layered, 10-layered and 18-layered CR multilayer laminates.

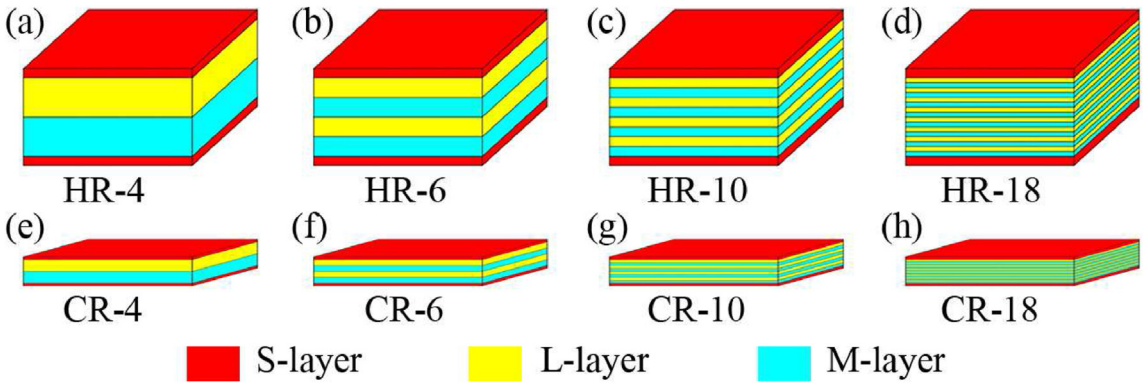

Fig. 1 – The schematic diagrams for HR and CR multilayer laminates. (a)–(d) 4-layered, 6-layered, 10-layered and 18-layered HR laminates, respectively. (e)–(h) 4-layered, 6-layered, 10-layered and 18-layered CR laminates, respectively. Red: 304 stainless steel. Yellow: Low C steel. Cyan: Medium-Mn steel.

2.2. *Experimental procedure*

The plate tensile specimens with dog-bone shape and gauge dimensions of 18 mm × 2.5 mm × 1.5 mm, were cut from the CRA sheets with longitudinal axis parallel to the rolling direction. The uniaxial quasi-static tensile tests were carried out using an MTS 973 testing machine operating at a strain rate of $5 \times 10^{-4}\ s^{-1}$ and at room temperature. A 10 mm extensometer was used to accurately control and measure the displacement during tensile tests. The tensile testing was performed more than three times for each condition to verify the reproducibility.

In-situ high energy X-ray diffraction (HE-XRD) measurements were carried out on the beam-line 11-ID-C, at the Advanced Photon Source (APS), Argonne National Laboratory. The detailed experimental set-up can be found in the previous research [36]. Dimensions of the tensile specimen in the gage part for the in-situ tension tests were 10 mm × 3 mm × 1.5 mm. During tensile loading, a monochromatic X-ray beam with energy ~105 keV (λ = 0.1173 nm) and beam size of 500 μm × 500 μm was used. A 2-D detector was placed about 1600 mm behind the tensile sample to record the scattering intensity. Crystallographic planes were determined from the diffraction patterns and the lattice strains were calculated from the change of the measured inter-planar spacing.

The distributions of Vickers micro-hardness across interfaces for various samples prior to and after tensile tests were also obtained on the polished sample surfaces using a Vickers diamond indenter under a load of 10 gf for 15 s dwell time. Five groups of measurements for each point were obtained, the average value was taken and the error bar was also provided.

Electron backscatter diffraction (EBSD) and transmission electron microscopy (TEM) were used to characterize the microstructures prior to and after tensile deformation. EBSD observations were performed utilizing a ZEISS Gemini 300 SEM with an EBSD detector. The minimum scanning step of 35 nm was used during the EBSD acquisition. The surfaces for EBSD observations were first grinded by sandpapers, and then polished by a 0.5 μm diamond polishing powder and a 20 nm SiO_2 aqueous suspension. TEM observations were performed utilizing a JEOL-2100F at 200 kV. The TEM samples were prepared and thinned by mechanically polishing first, followed by a twin-jet polishing using a solution of 5% perchloric acid and 95% ethanol at −40 °C and under 65 V. Scanning electron microscopy (SEM) was also used to characterize the fracture surface. SEM observations were performed utilizing a JSM-7001F.

3. Results and discussion

3.1. *Heterogeneous structure and hardness difference*

The Vickers micro-hardness distributions along the thickness direction for 6-layered, 10-layered and 18-layered CRA multilayer laminates prior to tensile deformation are displayed in Fig. 2(a). The hardness has a significant difference among the S-layer, the L-layer and the M-layer, which can generate GNDs at the area near the interface during deformation due to strain incompatibility [7,19,37–40]. The highest hardness is detected in the S-layer due to unrecrystallized grains during annealing process, which will be displayed later. Moreover, the hardness near the interface in each layer is different from that far from the interface. In the S-layer, the hardness at the area near the interface is higher than that far from the interface, due to C atom diffusion from either the L-layer or the M-layer into the S-layer, resulting in inhibited austenite recrystallization and increased hardness at the area near the interface for the S-layer [20]. However, the hardness of the L-layer and the M-layer at the area near the S-layer interfaces becomes lower as compared to those far from the interfaces. This phenomenon becomes inapparent with decreasing layer thickness, which can be attributed to a reduction of IAZ width [19,20] as shown in Fig. 2(b). Therefore, the hardness exhibits a gradient distribution on both sides of the interface. The average statistical hardness for each layer is calculated in Fig. 2(c) and the initial hardness is almost unaffected by the layer thickness. The hardness differences between S-layer/M-layer, S-layer/L-layer and M-layer/L-layer are also calculated in Fig. 2(d). It is evident that the significant hardness difference between the M-layer and the L-layer has been successfully designed in the present study.

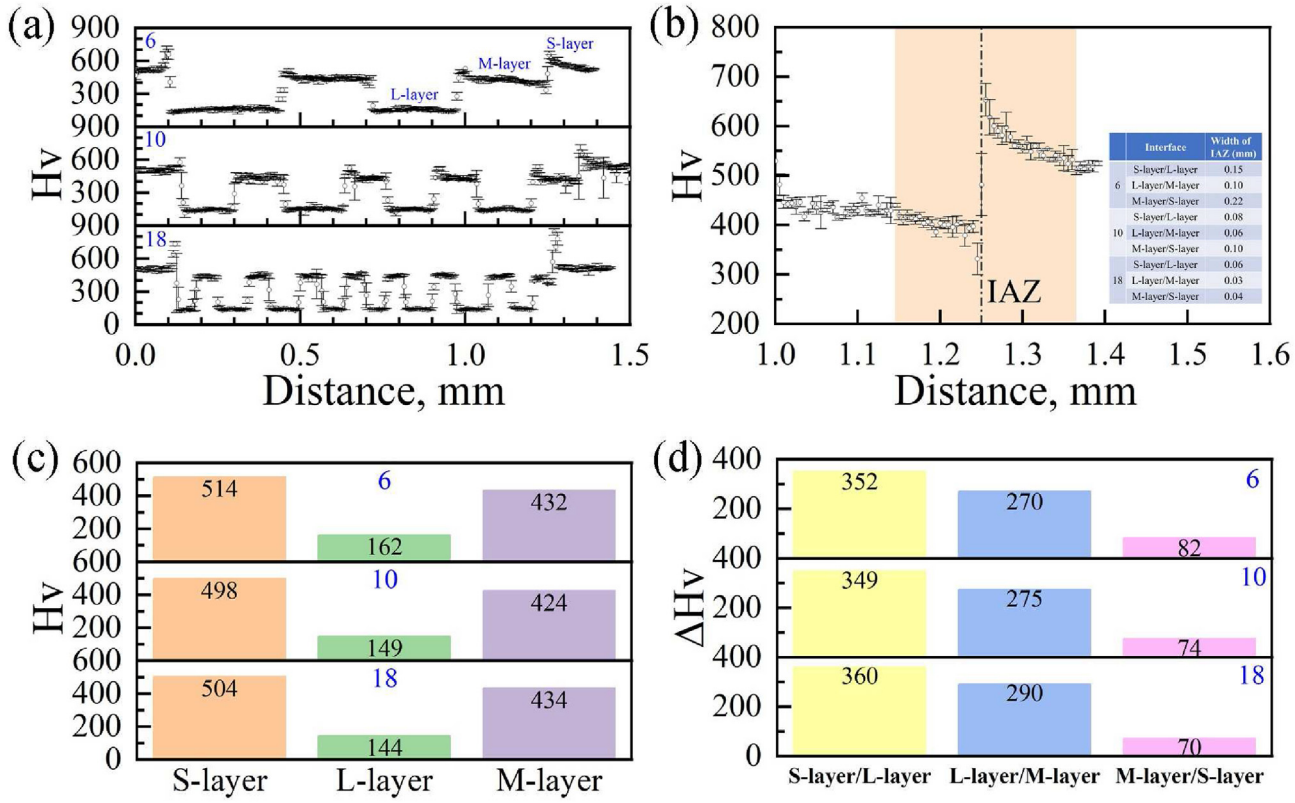

Fig. 2 – The Vickers micro-hardness distributions for CRA multilayer laminates prior to tensile deformation. (a) The hardness distributions along the thickness direction for 6-layered, 10-layered and 18-layered laminates. (b) The width of IAZ. (c) The average statistical hardness for the S-layer, the L-layer and the M-layer. (d) The average hardness differences between S-layer/L-layer, L-layer/M-layer and M-layer/S-layer.

The synchrotron HE-XRD patterns of 6-layered and 18-layered CRA laminates prior to tensile deformation are shown in Fig. 3. The diffraction peaks of α-ferrite and γ-austenite are clearly identified, and the close-up views of the small diffraction peaks of carbide are also displayed in the insets.

The density of GNDs can be estimated by the kernel average misorientation (KAM) value using a method based on the strain gradient theory, which was proposed by Gao and Kubin [38,41]:

$$\rho_{GND} = 2\theta/lb$$

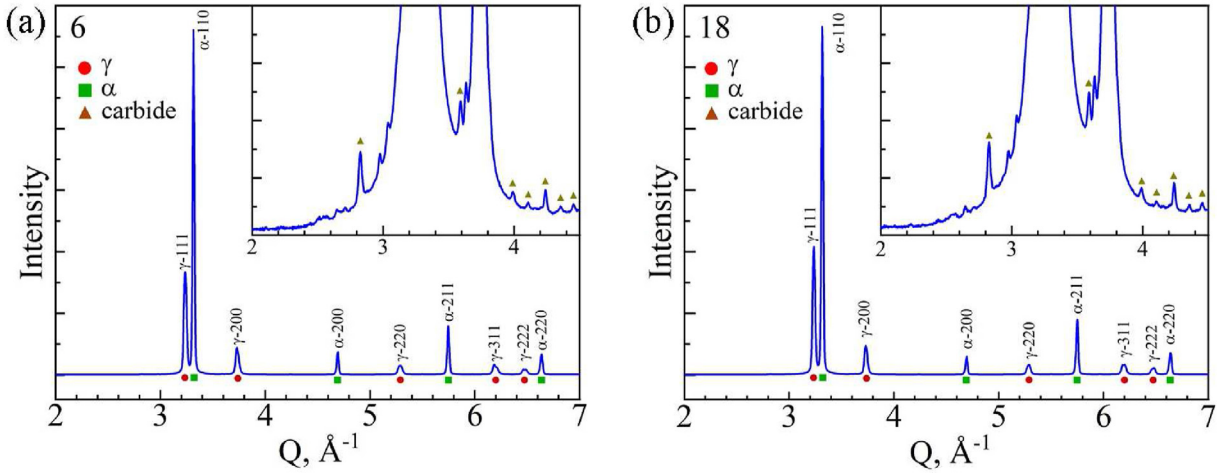

Fig. 3 – The synchrotron HE-XRD patterns of CRA multilayer laminates prior to tensile deformation: (a) The 6-layered laminate; (b) The 18-layered laminate.

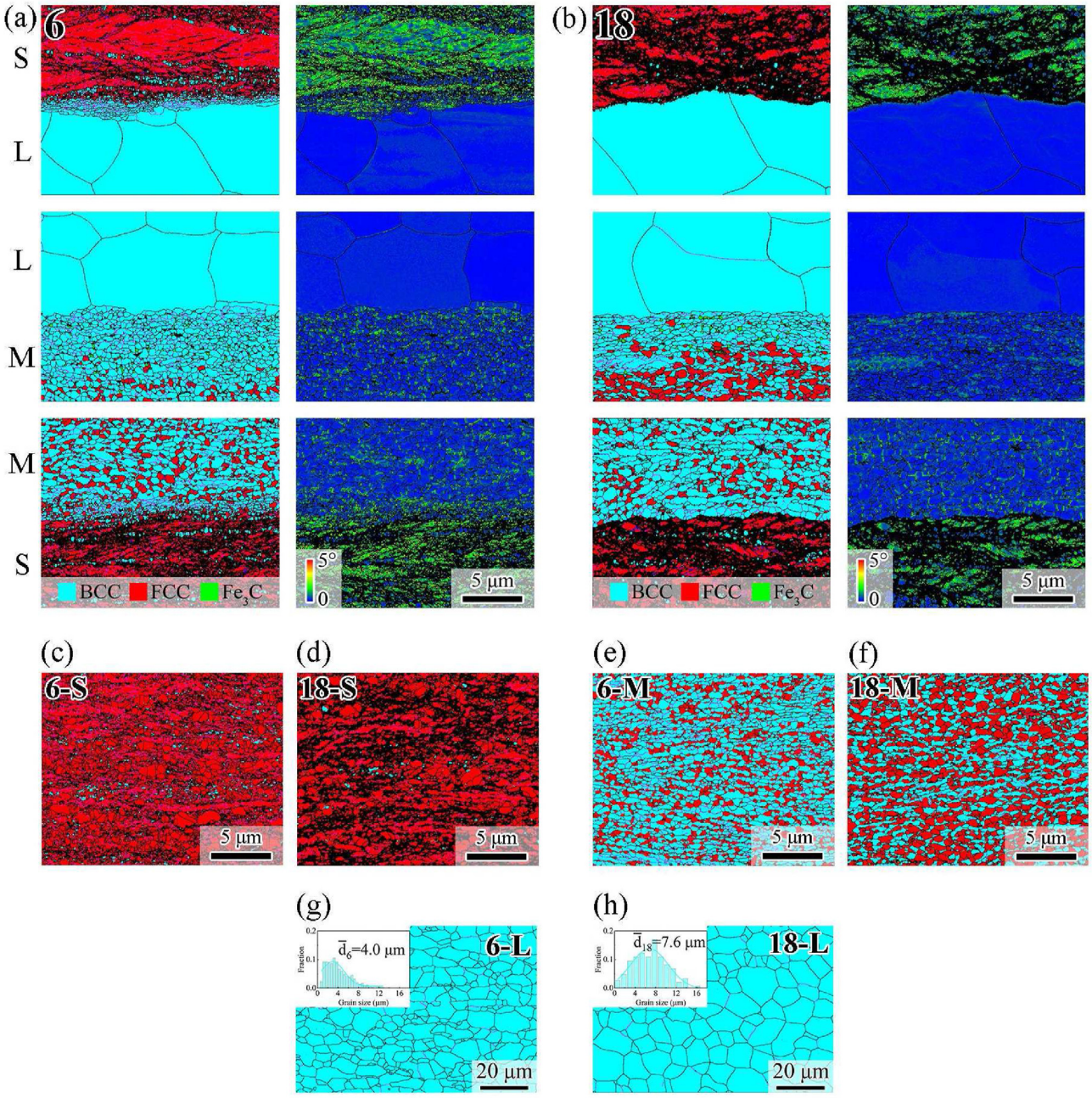

Fig. 4 – EBSD images for CRA multilayer laminates prior to tensile deformation. (a) and (b) Phase maps and corresponding KAM maps at the area near the interface for 6-layered and 18-layered laminates, respectively. (c) and (d) Phase maps with grain boundaries for S-layers at the area far from the interface in 6-layered and 18-layered laminates, respectively. (e) and (f) Phase maps with grain boundaries for M-layers at the area far from the interface in 6-layered and 18-layered laminates, respectively. (g) and (h) Phase maps with grain boundaries for L-layers at the area far from the interface in 6-layered and 18-layered laminates, respectively, and the grain size distributions are displayed in the insets.

where ρ_{GND} is the GND density at local points, θ is the misorientation at local points, l is the unit length for the local points, and b is Burger's vector for the materials.

Fig. 4 shows EBSD phase maps and KAM maps prior to tensile deformation. Fig. 4(a) and (b) show EBSD phase maps and corresponding KAM maps at the area near the interface. The interfaces can be easily identified in these figures, and the microstructures across the interfaces are highly heterogeneous. The microstructure of the S-layer at the area near the interface is only composed of unrecrystallized austenite with high density of GNDs, but the microstructure of the S-layer at the area far from the interface is mainly composed of partial recrystallized austenite and unrecrystallized austenite as shown in Fig. 4(c) and 4(d). The low resolution fraction of EBSD for the S-layer can be attributed to severe plastic deformation by cold rolling and non-recrystallization

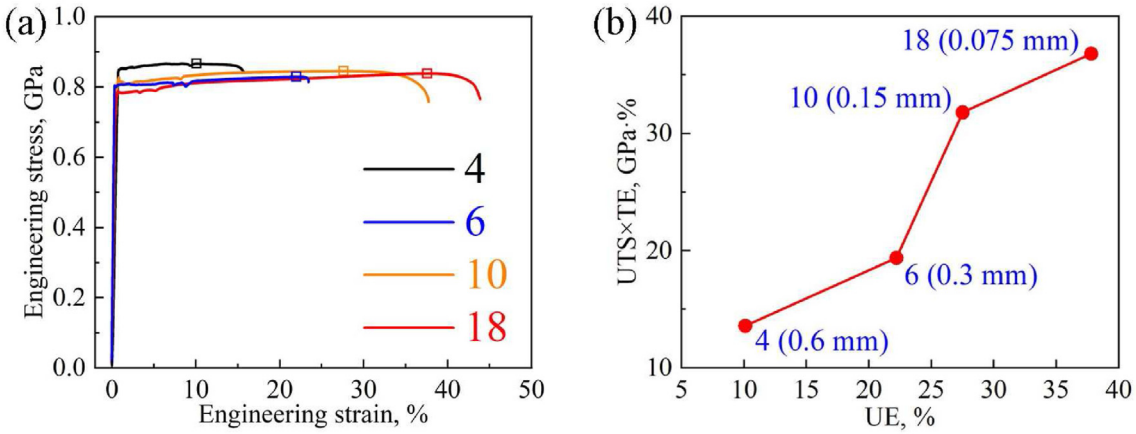

Fig. 5 – Tensile properties for CRA multilayer laminates. (a) Tensile engineering stress-strain curves. (b) Product of strength and total elongation (UTS × TE) versus uniform elongation (UE), in which the layer number and thickness for each sample are also indicated.

during intercritical annealing process. The microstructure of the M-layer mainly consists of austenite and ferrite as shown in Fig. 4(e) and (f), and the average grain sizes of austenite and ferrite are about 0.42 μm and 0.58 μm, respectively, for all multilayer laminates with different layer thickness. A little volume fraction of Fe_3C is only found in the M-layer. Austenite disappears and the microstructure of M-layer is mainly composed of ferrite at the area near the M-layer/L-layer interface, which could be due to the existence of IAZ. The width of zone without austenite decreases with decreasing layer thickness, which are about 6 μm and 3 μm for 6-layered and 18-layered laminates, respectively. The average volume fractions of austenite in M-layers significantly increase with decreasing layer thickness, which are about 28.6% and 49.2% for 6-layered and 18-layered laminates, respectively. Therefore, the ability of reverse transformation from martensite into austenite in the CR multilayer laminate during intercritically annealing is promoted with decreasing layer thickness. The microstructure of the L-layer is only composed of recrystallized ferrite as shown in Fig. 4(g) and (h), and the average grain sizes are about 4.0 μm and 7.6 μm for 6-layered and 18-layered laminates, respectively. These results reveal a significant microstructural difference between the M-layer and the L-layer.

3.2. *The effect of layer thickness on tensile properties*

Fig. 5(a) shows the tensile engineering stress-strain curves of the investigated multilayer laminates with different layer thickness. It is obvious that the ductility and the product of strength and elongation significantly increase with decreasing layer thickness, but the yield stress remains almost constant, as shown in Fig. 5. These observations indicate that a smaller layer thickness can result in more heterogeneous interfaces, which are beneficial for strain hardening and ductility. Thus, a better synergy of strength and ductility can be achieved for the samples with smaller layer thickness, the trade-off between the strength and ductility can be resolved by adjusting the layer thickness in the multilayer laminates. The stress plateau that occurs after the yield point, which is known as Lüders band, can be observed in tensile deformation for all multilayer laminates, due to the lack of mobile dislocations in the ultrafine grained microstructures of the S-layer and the M-layer, leading to insufficient strain hardening capacity. Deformation-induced martensitic transformation can be triggered once a critical plastic strain is achieved in the Lüders band region, resulting in the prevention of further strain localization [30,35,42]. After the Lüders band, a strain hardening stage is observed. Therefore, the shape of these tensile

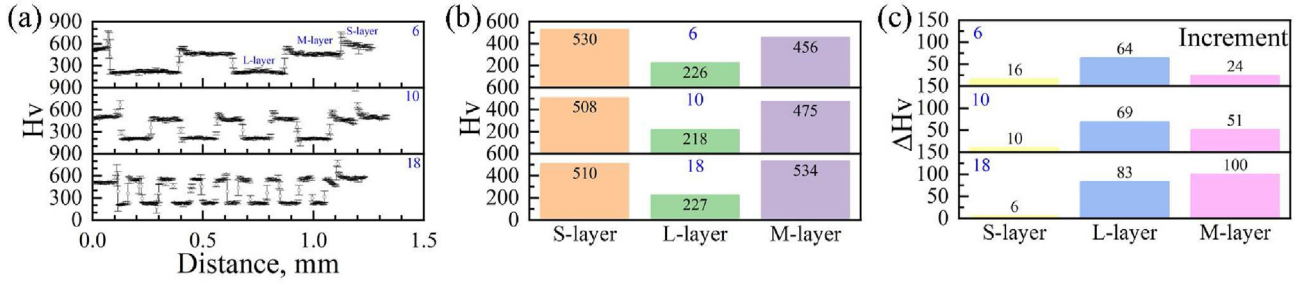

Fig. 6 – The Vickers micro-hardness measurements for CRA multilayer laminates after tensile deformation. (a) The hardness distributions along the thickness direction for 6-layered, 10-layered and 18-layered laminates. (b) The average statistical hardness for the S-layer, the L-layer and the M-layer. (c) The average hardness increment for each layer after tensile deformation.

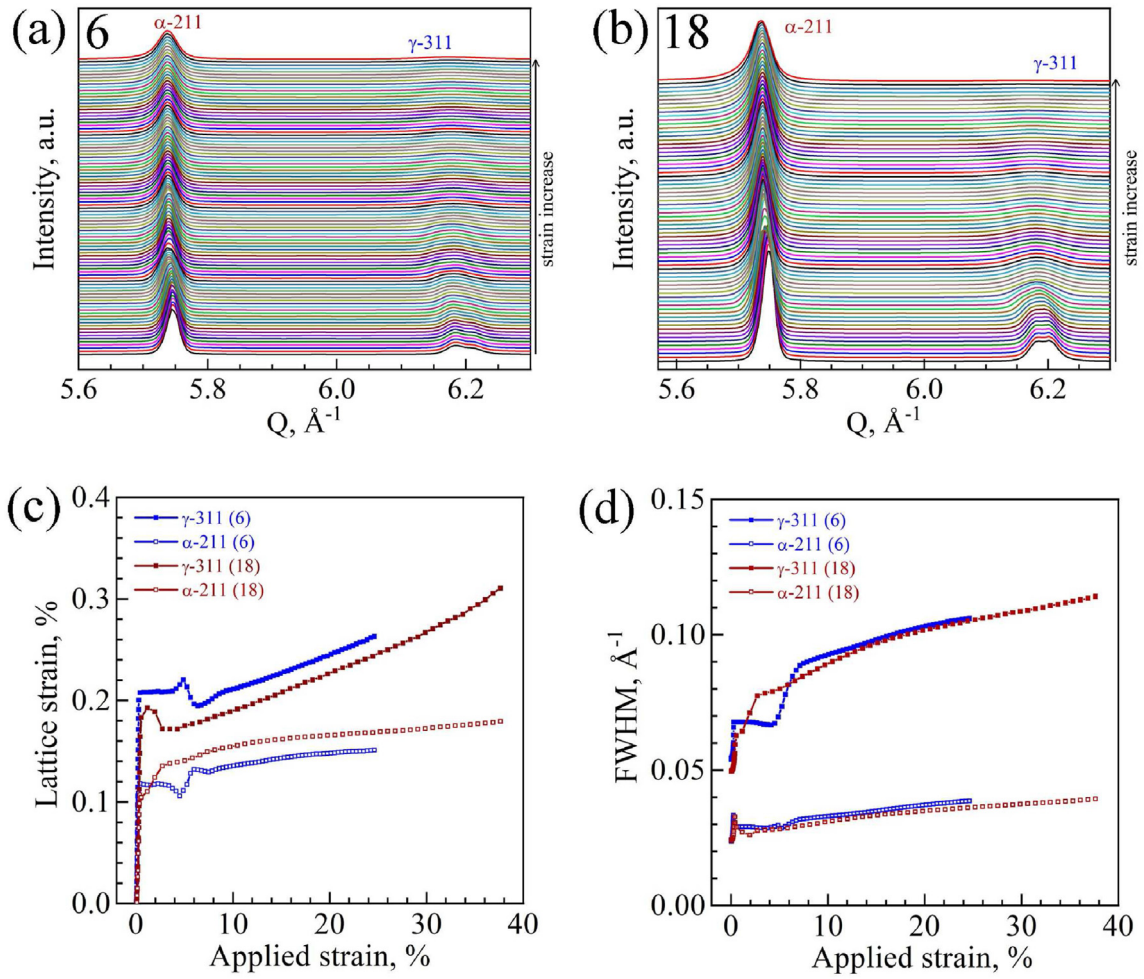

Fig. 7 – The in-situ HE-XRD measurements of 6-layered and 18-layered CRA laminates. (a) and (b) Diffraction peaks of $211_{\alpha/\alpha'}$ and 311_{γ} with increasing applied strains for 6-layered and 18-layered laminates, respectively. (c) The lattice strain of $211_{\alpha/\alpha'}$ and 311_{γ} planes versus applied strain. (d) The FWHM (dislocation density) of $211_{\alpha/\alpha'}$ and 311_{γ} planes versus applied strain.

curves may be attributed to the presence of the ultrafine grained microstructures of the S-layer and the M-layer.

3.3. *Deformation-induced martensite transformation and dislocation behavior*

After tensile deformation, the Vickers micro-hardness distributions along the thickness direction for 6-layered, 10-layered and 18-layered CRA multilayer laminates are displayed in Fig. 6(a). The average statistical hardness for each layer is calculated in Fig. 6(b), and the hardness increment for each layer prior to and after tensile deformation is calculated in Fig. 6(c). It is obvious that the hardness increases in every layer after tensile deformation. Moreover, the hardness increment for the M-layer significantly increases with decreasing layer thickness.

The microstructural evolution for 6-layered and 18-layered CRA laminates during tensile deformation are investigated by the in-situ synchrotron HE-XRD as shown in Fig. 7. An increase in full width at half maximum (FWHM) of the $211_{\alpha/\alpha'}$ and 311_{γ} diffraction peaks with increasing applied strains for 6-layered and 18-layered laminates are shown in Fig. 7(a) and (b), respectively. Fig. 7(c) shows the lattice strain evolution of $211_{\alpha/\alpha'}$ and 311_{γ} planes as a function of applied strain. After yielding, the difference in lattice strain between α/α' and γ indicates that load partitioning takes place. Moreover, more interfaces result in smaller difference in load partitioning between two phases. This could be attributed to the compatible deformation by interface, thus more interfaces can reduce the difference in load partitioning between two phases and significantly increase the ductility. Fig. 7(d) shows the FWHM (which can be expressed as dislocation density) evolution of $211_{\alpha/\alpha'}$ and 311_{γ} planes as a function of applied strain [41,43,44]. At the same applied strain, the dislocation densities for 6-layered and 18-layered CRA laminates are almost equal. Due to more interfaces, higher density of GNDs could be induced at interfaces. Thus, the difference in GND density between two phases is reduced and the deformation between two phases is more compatible, which can significantly increase the ductility.

Fig. 8(a)-8(f) show EBSD phase maps after tensile deformation. Fig. 8(a) and (b) show the area near the interface for 6-layered and 18-layered CRA laminates, respectively. Fig. 8(c) and (d) show S-layers at the area far from the interface for 6-

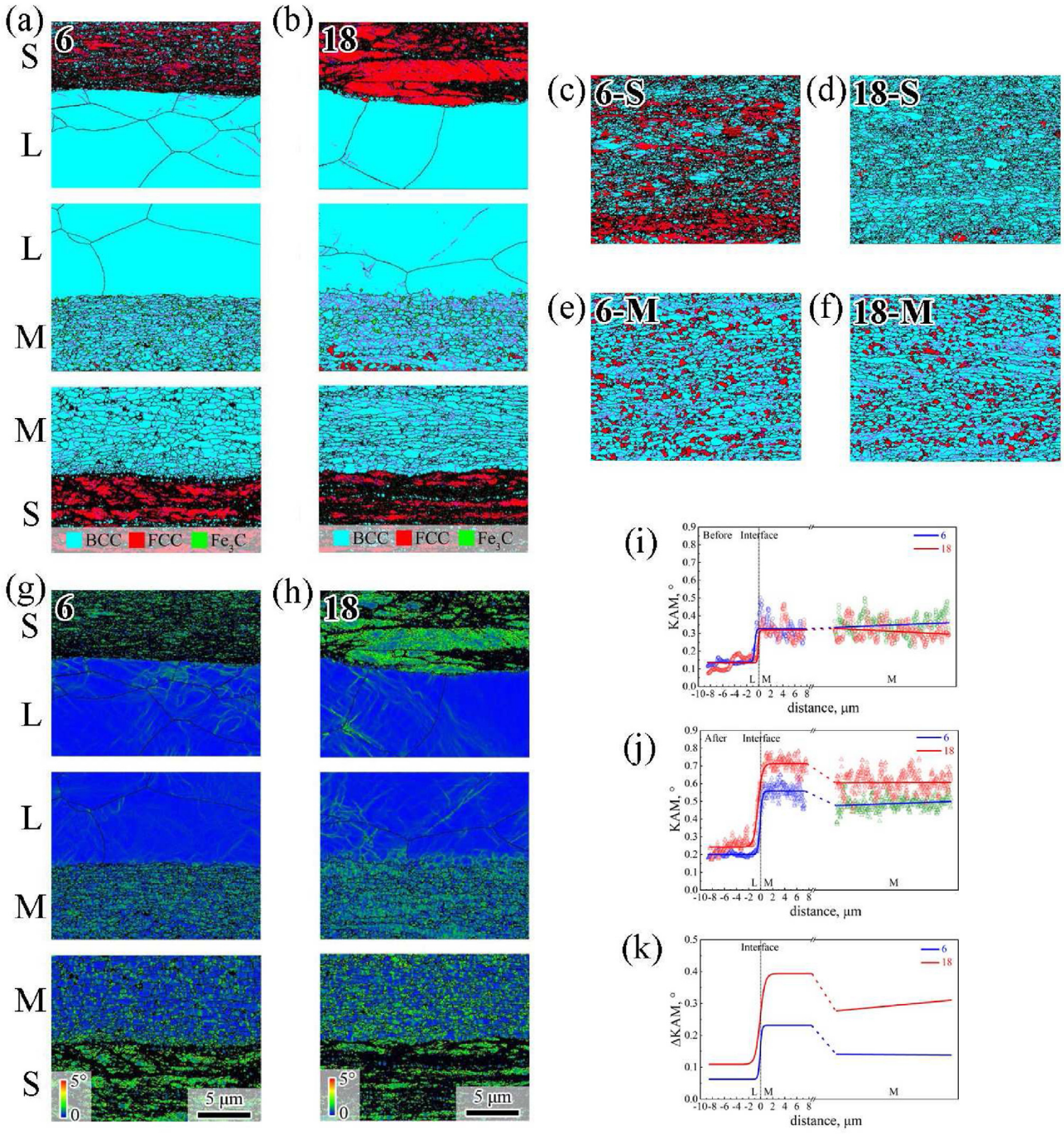

Fig. 8 – EBSD images for CRA multilayer laminates after tensile deformation. (a) and (b) Phase maps with grain boundaries at the area near the interface for 6-layered and 18-layered laminates, respectively. (c) and (d) Phase maps with grain boundaries for S-layers at the area far from the interface in 6-layered and 18-layered CRA laminates, respectively. (e) and (f) Phase maps with grain boundaries for M-layers at the area far from the interface in 6-layered and 18-layered CRA laminates, respectively. (g) and (h) KAM maps for 6-layered and 18-layered laminates, respectively. (i) and (j) The evolution of KAM values for M-layer/L-layer interfaces prior to and after tensile deformation, respectively. (k) The increments of KAM values for M-layer/L-layer interfaces prior to and after tensile deformation.

layered and 18-layered CRA laminates, respectively. Fig. 8(e) and (f) show M-layers for 6-layered and 18-layered CRA laminates, respectively. Deformation-induced martensite transformation is observed in M-layers and S-layers. The volume fractions of retained austenite for M-layers after tensile deformation are about 15.1% and 12.0% in 6-layered and 18-layered CRA laminates, respectively. Thus, the total volume fractions of deformation-induced martensite transformation for M-layers are about 13.5% and 37.2% in 6-layered and 18-layered CRA laminates, respectively. The volume fractions of

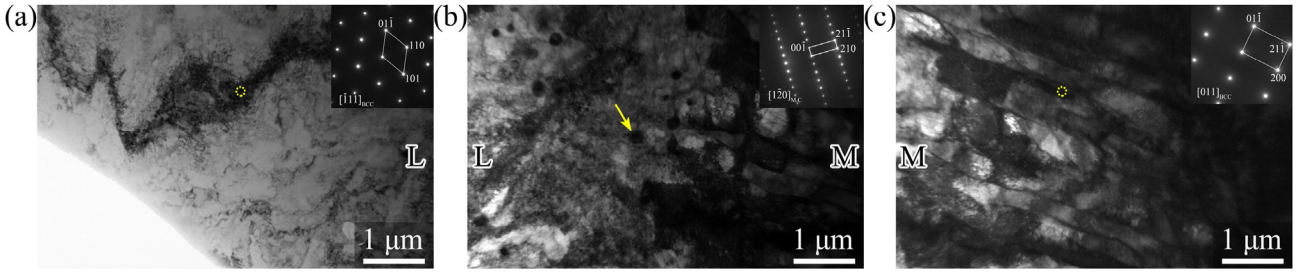

Fig. 9 – TEM images after tensile deformation for the 18-layered laminate at the area near the L-layer/M-layer interface. (a) L-layer; (b) L-layer/M-layer interface; (c) M-layer.

deformation-induced martensite transformation for S-layers are about 59.5% and 98.1% in 6-layered and 18-layered CRA laminates, respectively. Therefore, deformation-induced martensite transformation is significantly promoted with decreasing layer thickness, which can contribute to the larger ductility.

Strain partitioning across the interfaces should occur during the plastic deformation for the multilayer laminates, resulting in strong strain gradient at the area near the interfaces. Therefore, how the density of GNDs evolves prior to and after tensile deformation should be characterized. KAM maps at the area near the M-layer/L-layer interface after tensile deformation are shown in Fig. 8(g) and (h). Fig. 8(i) and (j) show the evolution of KAM values prior to and after tensile deformation, respectively. The increments of KAM value after tensile deformation are shown in Fig. 8(k). It is obvious that the increments of KAM values for M-layers are higher than that for L-layers, and the increments of KAM values for M-layers significantly increase with decreasing layer thickness, which are consistent with the result of hardness increments for M-layers as shown in Fig. 6(c). Moreover, the closer to the interface, the higher the KAM value after tensile deformation, which is consistent with the results of HE-XRD. GNDs can pile up at the area near the interface and among the various domains to accommodate the strain gradient and produce back stress in the soft domains and forward stress in the hard domains, which together produces the HDI stress [37,45–47]. The interface can promote the accumulation of dislocations,

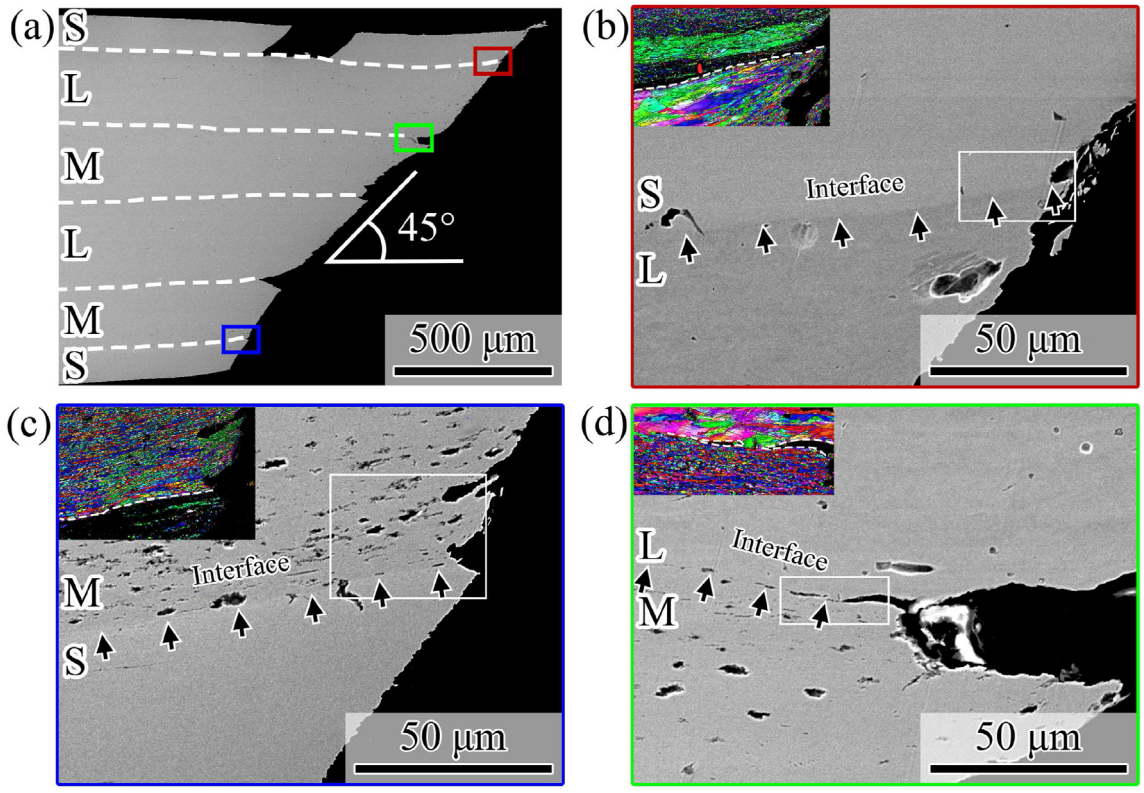

Fig. 10 – The SEM images for transverse direction of fracture section in the 6-layered laminate. (a) Fracture surface. (b)–(d) The close-up views of the S-layer/L-layer interface, the M-layer/S-layer interface and the L-layer/M-layer interface in (a), respectively. The insets in (b)–(d) are the IPF maps for the close-up views of corresponding interfaces.

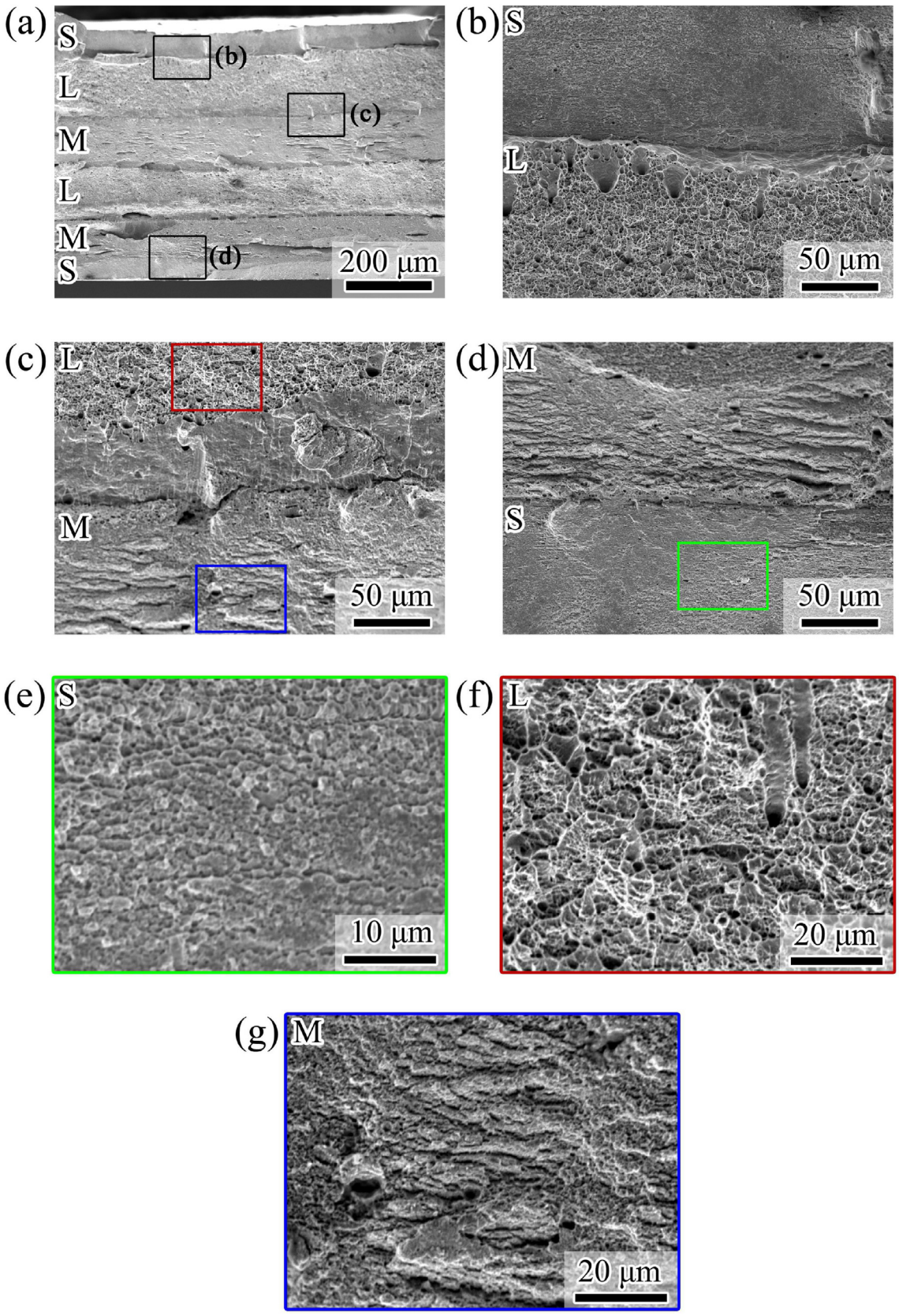

Fig. 11 – The SEM images for fracture morphology of the 6-layered laminate. (a) Fracture morphology. (b–d) The close-up views of the S-layer/L-layer interface, the L-layer/M-layer interface and the M-layer/S-layer interface in (a), respectively. (e–g) The close-up views of the S-layer, the L-layer and the M-layer, respectively.

which delocalizes the plastic strain and prevents the premature necking [48], the more interfaces, the better the mechanical properties, as shown in Fig. 5.

TEM images after tensile deformation for the 18-layered laminate at the area near the L-layer/M-layer interface are displayed in Fig. 9. High density dislocations are found in both L-layers and M-layers as shown in Fig. 9(a) and (c). It appears that the dislocation density of the M-layer after tensile deformation is significantly higher than that of the L-layer. The smaller grains with lamellar morphology are detected in the M-layer, while the larger grains are found in the L-layer. Furthermore, it is interesting to note that accumulation of abundant dislocations can be observed at the area near the M-layer/L-layer interface as shown in Fig. 9(b). These results reveal significant differences in microstructure and dislocation density between the two layers after tensile deformation. Meanwhile, the M_3C carbide can be shear by dislocations, which indicates the presence of dislocation behavior. Therefore, deformation-induced martensite transformation (Fig. 9(c)) and dislocation behaviors dominate the plastic deformation of multilayer laminates.

3.4. *Fracture mechanism*

The SEM images for transverse direction of fracture section in the 6-layered laminate are displayed in Fig. 10. The S-layer/L-layer interface bonding and the S-layer/M-layer interface bonding are relatively good, and the main cracks nucleate and propagate at the L-layer/M-layer interfaces. The interfaces are identified by IPF maps with close-up views, as shown in Fig. 10(b–d). The SEM images for fracture morphology of the 6-layered laminate are displayed in Fig. 11. A significant crack is identified at the L-layer/M-layer interface as illustrated in Fig. 11(c), while the S-layer/L-layer interface and the M-layer/S-layer interface are almost intact, as illustrated in Fig. 11(b) and (d). Larger dimples are typically observed in L-layers, while smaller ones are commonly found in S-layers. These observations are consistent with the grain sizes of these layers. Moreover, plastic tearing features can be identified in M-layers. The crack propagation requires energy consumption during the micro-fracture process [41], so the more interfaces, the more energy consumption, the better performance.

4. Conclusions

In summary, the ductility and the product of strength and elongation are observed to significantly increase with decreasing layer thickness in multilayer laminates, but the yield stress remains almost constant.

1) Transformation-induced-plasticity effect plays an important role in plastic deformation and provides strain hardening, deformation-induced martensite transformation is significantly promoted with decreasing layer thickness.
2) Geometrically necessary dislocations can pile up at the area near the interface, therefore, the interface can promote the accumulation of dislocations, which delocalizes the plastic strain and prevents the premature necking. Thus, the more interfaces can result in better mechanical properties.
3) The main cracks nucleate and propagate at the low C steel layer and the medium-Mn steel layer interfaces. The crack propagation requires energy consumption during the micro-fracture process, so the more interfaces, the more energy consumption, the better performance. The present results provide insights and procedures to improve ductility without sacrifice of strength in the heterogeneous multilayer laminates.

Data availability

All data used during this study are available from the corresponding author by request.

Declaration of competing interest

The authors declare that they have no known competing financial interests or personal relationships that could have appeared to influence the work reported in this paper.

Acknowledgements

This research was supported by the NSFC Basic Science Center Program for “Multiscale Problems in Nonlinear Mechanics” [grant number 11988102] and the National Natural Science Foundation of China [grant number 52192591].

REFERENCES

[1] Zhu YT, Liao XZ. Nanostructured metals - retaining ductility. Nat Mater 2004;3:351–2.
[2] Valiev R. Nanostructuring of metals by severe plastic deformation for advanced properties. Nat Mater 2004;3:511–6.
[3] Valiev RZ, Alexandrov IV, Zhu YT, Lowe TC. Paradox of strength and ductility in metals processed by severe plastic deformation. J Mater Res 2002;17:5–8.
[4] Meyers MA, Mishra A, Benson DJ. Mechanical properties of nanocrystalline materials. Prog Mater Sci 2006;51:427–556.
[5] Fang TH, Li WL, Tao NR, Lu K. Revealing extraordinary intrinsic tensile plasticity in gradient nano-grained copper. Science 2011;331:1587–90.
[6] Zeng Z, Li XY, Xu DS, Lu L, Gao HJ, Zhu T. Gradient plasticity in gradient nano-grained metals. Extreme Mech Lett 2016;8:213–9.
[7] Wu XL, Jiang P, Chen L, Yuan FP, Zhu YTT. Extraordinary strain hardening by gradient structure. Proc Natl Acad Sci U S A 2014;111:7197–201.
[8] Pan QS, Zhang LX, Feng R, Lu QH, An K, Chuang AC, et al. Gradient cell-structured high-entropy alloy with exceptional strength and ductility. Science 2021;374:984.
[9] Wang YM, Chen MW, Zhou FH, Ma E. High tensile ductility in a nanostructured metal. Nature 2002;419:912–5.
[10] Yang MX, Yan DS, Yuan FP, Jiang P, Ma E, Wu XL. Dynamically reinforced heterogeneous grain structure

prolongs ductility in a medium-entropy alloy with gigapascal yield strength. Proc Natl Acad Sci U S A 2018;115:7224–9.
[11] Zhao YH, Topping T, Bingert JF, Thornton JJ, Dangelewicz AM, Li Y, et al. High tensile ductility and strength in bulk nanostructured nickel. Adv Mater 2008;20:3028–33.
[12] Wu XL, Yuan FP, Yang MX, Jiang P, Zhang CX, Chen L, et al. Nanodomained nickel unite nanocrystal strength with coarse-grain ductility. Sci Rep 2015;5:10.
[13] Wu XL, Yang MX, Yuan FP, Wu GL, Wei YJ, Huang XX, et al. Heterogeneous lamella structure unites ultrafine-grain strength with coarse-grain ductility. Proc Natl Acad Sci U S A 2015;112:14501–5.
[14] Yuan R, Beyerlein IJ, Zhou CZ. Homogenization of plastic deformation in heterogeneous lamella structures. Mater Res Lett 2017;5:251–7.
[15] Ma XL, Huang CX, Xu WZ, Zhou H, Wu XL, Zhu YT. Strain hardening and ductility in a coarse-grain/nanostructure laminate material. Scripta Mater 2015;103:57–60.
[16] Ma XL, Huang CX, Moering J, Ruppert M, Hoppel HW, Goken M, et al. Mechanical properties of copper/bronze laminates: role of interfaces. Acta Mater 2016;116:43–52.
[17] Wu H, Fan GH, Huang M, Geng L, Cui XP, Xie HL. Deformation behavior of brittle/ductile multilayered composites under interface constraint effect. Int J Plast 2017;89:96–109.
[18] Beyerlein IJ, Mayeur JR, Zheng SJ, Mara NA, Wang J, Misra A. Emergence of stable interfaces under extreme plastic deformation. Proc Natl Acad Sci U S A 2014;111:4386–90.
[19] Huang CX, Wang YF, Ma XL, Yin S, Hoppel HW, Goken M, et al. Interface affected zone for optimal strength and ductility in heterogeneous laminate. Mater Today 2018;21:713–9.
[20] He JY, Ma Y, Yan DS, Jiao SH, Yuan FP, Wu XL. Improving ductility by increasing fraction of interfacial zone in low C steel/304 SS laminates. Mater Sci Eng, A 2018;726:288–97.
[21] Li DY, Fan GH, Huang XX, Jensen DJ, Miao KS, Xu C, et al. Enhanced strength in pure Ti via design of alternating coarse- and fine-grain layers. Acta Mater 2021;206:13.
[22] Yang MX, Pan Y, Yuan FP, Zhu YT, Wu XL. Back stress strengthening and strain hardening in gradient structure. Mater Res Lett 2016;4:145–51.
[23] Zhu YT, Wu XL. Perspective on hetero-deformation induced (HDI) hardening and back stress. Mater Res Lett 2019;7:393–8.
[24] Zheng SJ, Beyerlein IJ, Carpenter JS, Kang KW, Wang J, Han WZ, et al. High-strength and thermally stable bulk nanolayered composites due to twin-induced interfaces. Nat Commun 2013;4:8.
[25] Ojima M, Inoue J, Nambu S, Xu PG, Akita K, Suzuki H, et al. Stress partitioning behavior of multilayered steels during tensile deformation measured by in situ neutron diffraction. Scripta Mater 2012;66:139–42.
[26] Misra A, Hirth JP, Hoagland RG. Length-scale-dependent deformation mechanisms in incoherent metallic multilayered composites. Acta Mater 2005;53:4817–24.
[27] Jacques PJ. Transformation-induced plasticity for high strength formable steels. Curr Opin Solid State Mater Sci 2004;8:259–65.
[28] Fischer FD, Reisner G, Werner E, Tanaka K, Cailletaud G, Antretter T. A new view on transformation induced plasticity (TRIP). Int J Plast 2000;16:723–48.
[29] Yuan FP, Bian XD, Jiang P, Yang MX, Wu XL. Dynamic shear response and evolution mechanisms of adiabatic shear band in an ultrafine-grained austenite-ferrite duplex steel. Mech Mater 2015;89:47–58.
[30] Wang W, Liu YK, Zhang ZH, Yang MX, Zhou LL, Wang J, et al. Deformation mechanisms for a new medium-Mn steel with 1.1 GPa yield strength and 50% uniform elongation. J Mater Sci Technol 2023;132:110–8.
[31] Das A, Tarafder S. Experimental investigation on martensitic transformation and fracture morphologies of austenitic stainless steel. Int J Plast 2009;25:2222–47.
[32] Huang CX, Yang G, Wang C, Zhang ZF, Wu SD. Mechanical behaviors of ultrafine-grained 301 austenitic stainless steel produced by equal-channel angular pressing. Metall Mater Trans A 2011;42A:2061–71.
[33] Lebedev AA, Kosarchuk VV. Influence of phase transformations on the mechanical properties of austenitic stainless steels. Int J Plast 2000;16:749–67.
[34] Xing JX, Yuan FP, Wu XL. Enhanced quasi-static and dynamic shear properties by heterogeneous gradient and lamella structures in 301 stainless steels. Mater Sci Eng, A 2017;680:305–16.
[35] Sohrabi MJ, Mirzadeh H, Sadeghpour S, Mahmudi R. Grain size dependent mechanical behavior and TRIP effect in a metastable austenitic stainless steel. Int J Plast 2023;160:18.
[36] Cheng S, Wang YD, Choo H, Wang XL, Almer JD, Liaw PK, et al. An assessment of the contributing factors to the superior properties of a nanostructured steel using in situ high-energy X-ray diffraction. Acta Mater 2010;58:2419–29.
[37] Wu XL, Zhu YT. Heterogeneous materials: a new class of materials with unprecedented mechanical properties. Mater Res Lett 2017;5:527–32.
[38] Gao H, Huang Y, Nix WD, Hutchinson JW. Mechanism-based strain gradient plasticity - I. Theory. J Mech Phys Solid 1999;47:1239–63.
[39] Kubin LP, Mortensen A. Geometrically necessary dislocations and strain-gradient plasticity: a few critical issues. Scripta Mater 2003;48:119–25.
[40] Ashby MF. Deformation of plastically NON-homogeneous materials. Phil Mag 1970;21:399.
[41] Liu L, Yu Q, Wang Z, Ell J, Huang MX, Ritchie RO. Making ultrastrong steel tough by grain-boundary delamination. Science 2020;368:1347.
[42] Gao S, Bai Y, Zheng RX, Tian YZ, Mao WQ, Shibata A, et al. Mechanism of huge Luders-type deformation in ultrafine grained austenitic stainless steel. Scripta Mater 2019;159:28–32.
[43] Ungar T, Gubicza J, Ribarik G, Borbely A. Crystallite size distribution and dislocation structure determined by diffraction profile analysis: principles and practical application to cubic and hexagonal crystals. J Appl Crystallogr 2001;34:298–310.
[44] Ungar T, Dragomir I, Revesz A, Borbely A. The contrast factors of dislocations in cubic crystals: the dislocation model of strain anisotropy in practice. J Appl Crystallogr 1999;32:992–1002.
[45] Wu XL, Jiang P, Chen L, Zhang JF, Yuan FP, Zhu YT. Synergetic strengthening by gradient structure. Mater Res Lett 2014;2:185–91.
[46] Fang X, Xue QQ, Yu KY, Li RG, Jiang DQ, Ge L, et al. Superior strength-ductility synergy by hetero-structuring high manganese steel. Mater Res Lett 2020;8:417–23.
[47] Zhu YT, Wu XL. Heterostructured materials. Prog Mater Sci 2023;131:55.
[48] Wu H, Fan GH. An overview of tailoring strain delocalization for strength-ductility synergy. Prog Mater Sci 2020;113:51.